PHYSICAL REVIEW B **108**, 075113 (2023)

Spin-phonon-charge coupling in the two-dimensional honeycomb lattice compound $Ni_2Te_3O_8$

Ajay Tiwari,[1] D. Chandrasekhar Kakarla,[1,*] Bommareddy Poojitha,[2] Priyambada Sahoo,[3] H. L. Liu,[2] A. Dixit,[3]
C. W. Wang,[4] T. W. Yen,[1] M.-J. Hsieh,[5] J.-Y. Lin,[5,6] Jyothinagaram Krishnamurthy,[7] Y. C. Lai,[4] H. Chou,[1]
T. W. Kuo,[1] Arkadeb Pal,[1] and H. D. Yang[1,8,†]
[1]*Department of Physics, National Sun Yat-sen University, Kaohsiung 80424, Taiwan*
[2]*Department of Physics, National Taiwan Normal University, Taipei 11677, Taiwan*
[3]*Advanced Materials and Devices (A-MAD) Laboratory, Department of Physics,*
Indian Institute of Technology Jodhpur, Rajasthan 342037, India
[4]*National Synchrotron Radiation Research Center, Hsinchu 30076, Taiwan*
[5]*Institute of Physics, National Yang Ming Chiao Tung University, Hsinchu 30010, Taiwan*
[6]*Center for Emergent Functional Matter Science, National Yang Ming Chiao Tung University, Hsinchu 30010, Taiwan*
[7]*Department of Physics, School of Sciences, National Institute of Technology, Andhra Pradesh 534101, India*
[8]*Center of Crystal Research, National Sun Yat-sen University, Kaohsiung 80424, Taiwan*

(Received 8 December 2022; revised 3 July 2023; accepted 20 July 2023; published 4 August 2023)

A two-dimensional honeycomb-structured magnet $Ni_2Te_3O_8$ was synthesized, characterized, and comprehensively investigated for its intriguing physical properties. DC magnetization, specific heat, and neutron diffraction revealed a long-range commensurate antiferromagnetic ordering at $T_N \sim 35$ K with a propagation vector $\mathbf{k} = (100)$. The magnetic sublattice comprises stacking distorted honeycomb layers along the a axis. The Ni^{2+} spins on the honeycomb lattice are essentially pointing out of the layers and are antiferromagnetically coupled to the neighboring spins. Temperature (T) and magnetic field (H) dependent dielectric measurements indicated an apparent anomaly near T_N, accompanied by a weak magnetodielectric effect. Raman mode renormalization and lattice anomalies near T_N demonstrated spin-lattice coupling through magnetoelastic and spin-phonon interactions. These findings highlight the fascinating interplay between spin, charge, and phonon degrees of freedom in $Ni_2Te_3O_8$.

DOI: 10.1103/PhysRevB.108.075113

I. INTRODUCTION

Low-dimensional magnetic lattices and geometrically frustrated systems have attracted a flurry of research interest in the past few years owing to their potential to achieve nontrivial magnetic structures and spin-induced magnetoelectric effect [1–3]. Low-dimensional magnetic systems, including spin chains, spin dimers, spin ladders, and two-dimensional (2D) layers with kagome, pyrochlore, square, triangle, and honeycomb lattice motifs, exhibit a wide range of fascinating quantum phenomena, such as quantum spin-liquid states, Bose-Einstein condensation, spin-Peierls transitions, spin-glass states, and multiferroicity [4–10]. In 2D antiferromagnets (AFMs) such as layered honeycomb magnetic lattices with geometrical frustration, collective physical behavior is favored, such as the novel spin-liquid state proposed by Kitaev in $4d$ and $5d$ electrons. The Kitaev spin-liquid model has been proposed in several honeycomb magnets, including $\alpha-RuCl_3$, A_2IrO_3, and $NaNi_2BiO_{6-\delta}$. Recently, this model has been extended to materials with a d^7 configuration, characterized by the $t_{2g}^5e_g^2$ electronic configuration and the presence of high-spin Co^{2+} ions in $Li_3Co_2SbO_6$, $Na_3Co_2SbO_6$, and $Na_2Co_2TeO_6$ [11–23].

Recently, multiple potential strategies have been utilized to synthesize several low-dimensional magnetic lattices, such as oxides with lone-pair ions or oxyhalides [24]. Tellurium-centered magnetic systems are fascinating due to their variable oxidation states and broad coordination geometries, resulting in a remarkable variety of physical properties [24]. Recently, several $NiO-TeO_2$ binary phase diagram compounds have attracted research interest because of their complicated magnetic properties and the interesting dimensionality of the magnetic lattice. Table I summarizes the crystal structure, low-dimensional magnetic-ion configuration, and tellurium ions oxidation states. In this series, Ni_3TeO_6 is a well-established polar noncentrosymmetric magnetoelectric compound with $T_N = 52$ K. The spin structure of Ni_3TeO_6 consists of three inequivalent crystallographic Ni^{2+} sites with collinear ↑↑↓↓↑↑ spin chains along the hexagonal c axis [25]. $NiTe_2O_5$ has received significant interest because of its unconventional 2D magnetic critical behavior with $T_N = 30.5$ K despite having a quasi-one-dimensional spin-chain configuration of Ni^{2+} magnetic ions [26]. Recent nuclear magnetic resonance findings indicate the persistence of the Ising-like spin correlation in the paramagnetic region of $NiTe_2O_5$ [27]. A spin-charge-lattice coupling was established on a single crystal of $NiTe_2O_5$ below T_N [8]. The $Ni_2Te_3O_8$ belongs to the $NiO-TeO_2$ binary phase diagram, and its physical properties have yet to be determined.

The $A_2Te_3O_8$ (A = Ni, Co, Mn, and Zn) family of materials has a crystal structure belonging to the spiroffite mineral.

---

[*] Corresponding author: chandu@mail.nsysu.edu.tw
[†] Corresponding author: yang@mail.nsysu.edu.tw

TABLE I. List of materials from NiO−TeO_2 binary phase. SG, DML, DEML, and OST denote the space group, dimensionality of magnetic ions in the lattice, the dimensionality of experimental observation for the magnetic lattice, and the oxidation states of Te ions, respectively.

Sample	Structure	SG	T_N/T_D(K)	DML	DEML	OST	Reference
$NiTe_2O_5$	Orthorhombic	*Pbnm*	30	Quasi-1D spin chain	2D	Te^{4+}	[8,26]
Ni_3TeO_6	Trigonal	*R*3	52	3D crystal lattice	3D	Te^{6+}	[25]
$Ni_2Te_3O_8$	Monoclinic	*C*2/*c*	35	2D layered honeycomb	3D	Te^{4+}	[28]

The structure comprises ions in unusual oxidation states (A^{2+} and Te^{4+}) [28]. The structure consists of two-dimensional (2D) slabs containing $Te2_2O_6$ groups and A^{2+} cations and are connected by a $Te1O_4$ buffer layer. The distorted honeycomb lattice formed by the magnetic A^{2+} ions makes it an intriguing system to explore the magnetic properties of these materials. The recent study on $Co_2Te_3O_8$ under high pressure, using various probes such as x-ray diffraction, Raman spectroscopy, and UV-vis absorption spectroscopy, has revealed the versatility of these materials in exploring the complex interplay between crystal-field strength and spin-state transition [29]. These observations further motivated us to gain deeper insights into the structural and physical properties of these systems. This article comprehensively studies $Ni_2Te_3O_8$ through structural, magnetic, and dielectric measurements and low-*T* Raman scattering. The study reveals that $Ni_2Te_3O_8$ exhibits spin-phonon-charge coupling below T_N. Additionally, the structural and physical properties of $NiTe_2O_5$, Ni_3TeO_6, and $Ni_2Te_3O_8$ have been compared to identify similarities and differences. This analysis provides valuable insights into the behavior of this family of materials and highlights the potential for further research in this area.

II. EXPERIMENTAL METHODS

A polycrystalline $Ni_2Te_3O_8$ sample was synthesized using conventional solid-state methods, as reported in Ref. [30]. The quality of the polycrystalline $Ni_2Te_3O_8$ sample was evaluated at room temperature using high-resolution synchrotron x-ray diffraction (SXRD) with the 19A beamline of the Taiwan Photon Source (TPS 19A) at the National Synchrotron Radiation Research Center (NSRRC), Taiwan. For the SXRD measurements, the $Ni_2Te_3O_8$ polycrystals were crushed into a fine powder, and the sample was loaded in a quartz capillary of 0.3 mm diameter. Two sets of data were collected using the LN_2 cryostream (100–300 K; $\lambda = 0.77489$ Å) and the LHe Dynaflow cryostat (20–110 K; $\lambda = 0.61992$ Å). The data were collected using the Debye-Scherrer geometry and a double-crystal monochromator Si (111) with an energy resolution of 1.33×10^{-4}. Diffraction data were collected in the 2°–120° range in steps of 0.004°. Rietveld refinement of the SXRD data was performed using the FULLPROF suite software [31]. The crystal structure was analyzed using VESTA (version 3.5.2) software [32] with the VESTA file obtained from refinement.

All magnetic measurements were conducted using a magnetic property measurement system (MPMS-XL7) with an *H* up to 7 T. A flat pellet of approximately 2 mm ×2 mm ×0.5 mm was chosen for the dielectric measurements. Silver paint was used as the electrode on both sides of the crystal to form a parallel-plate capacitor. Dielectric (ε') measurements were performed using an Agilent E4980A precision *LCR* meter with an excitation AC voltage of 10 V. *T*- and *H*-dependent dielectric measurements were performed with a homemade sample probe in a Quantum Design MPMS system.

Neutron diffraction (ND) measurements below (3 K) and above (40 K) T_N were performed on a high-resolution powder diffractometer Echidna [33]. Neutron powder diffraction (NPD) measurements were performed on the ground powder samples using an incident wavelength of $\lambda = 2.4395$ Å (13.76 meV) defined by pyrolytic Ge (331) crystals at the monochromator position, with a take-off angle of 140°. The magnetic order parameter was determined using a cold neutron triple-axis spectrometer Sika at the Bragg Institute, ANSTO [34,35]. Sika was operated in the diffraction mode, where the energy of the neutrons was defined by PG (002) crystals at both the monochromator and analyzer positions using a fixed final energy of 3 meV(5.22 Å), and a Be filter was used to suppress higher-order contaminations. The (−102) magnetic Bragg reflection profiles were measured as a function of *T*, and the integrated intensities extracted by fitting them to the Gaussian peak function were used for obtaining the critical exponent of magnetic order. For ND measurements, approximately 10 g of the powdered sample was loaded into an aluminum sample holder filled with helium gas to facilitate thermal conduction. The *T* of the sample was controlled using a closed-cycle cryocooler.

Specific heat with temperature (C_P vs *T*) measurements were performed using a heat-pulsed thermal relaxation calorimeter in a physical property measurement system (PPMS). Micro-Raman scattering spectra were collected in a backscattering geometry using a 532 nm laser and a Senterra spectrometer equipped with a 1024-pixel-wide charge-coupled detector. The spectral resolution achieved using these instruments is generally less than $0.5\,\mathrm{cm}^{-1}$. The laser power was maintained at less than 0.2 mW to avoid local heating effects. The sample was mounted in a continuous-flow helium cryostat, which allowed temperature-dependent measurements between 5 and 300 K [36]. The detailed *ab initio* numerical calculation for phonon density of states has been described in the Supplemental Material [37]. The electron correlation interaction (Hubbard *U*) parameter for the Ni atom was taken from Ref. [38].

III. RESULTS AND DISCUSSION

A. Crystal structure

The SXRD at 300 K with Rietveld refinement for polycrystalline $Ni_2Te_3O_8$ is shown in Fig. 1(a), which was refined using the *C*2/*c* space group (No.15) with a monoclinic structure without any observed impurity phases. The structural refinement parameters are tabulated in the Supplemental

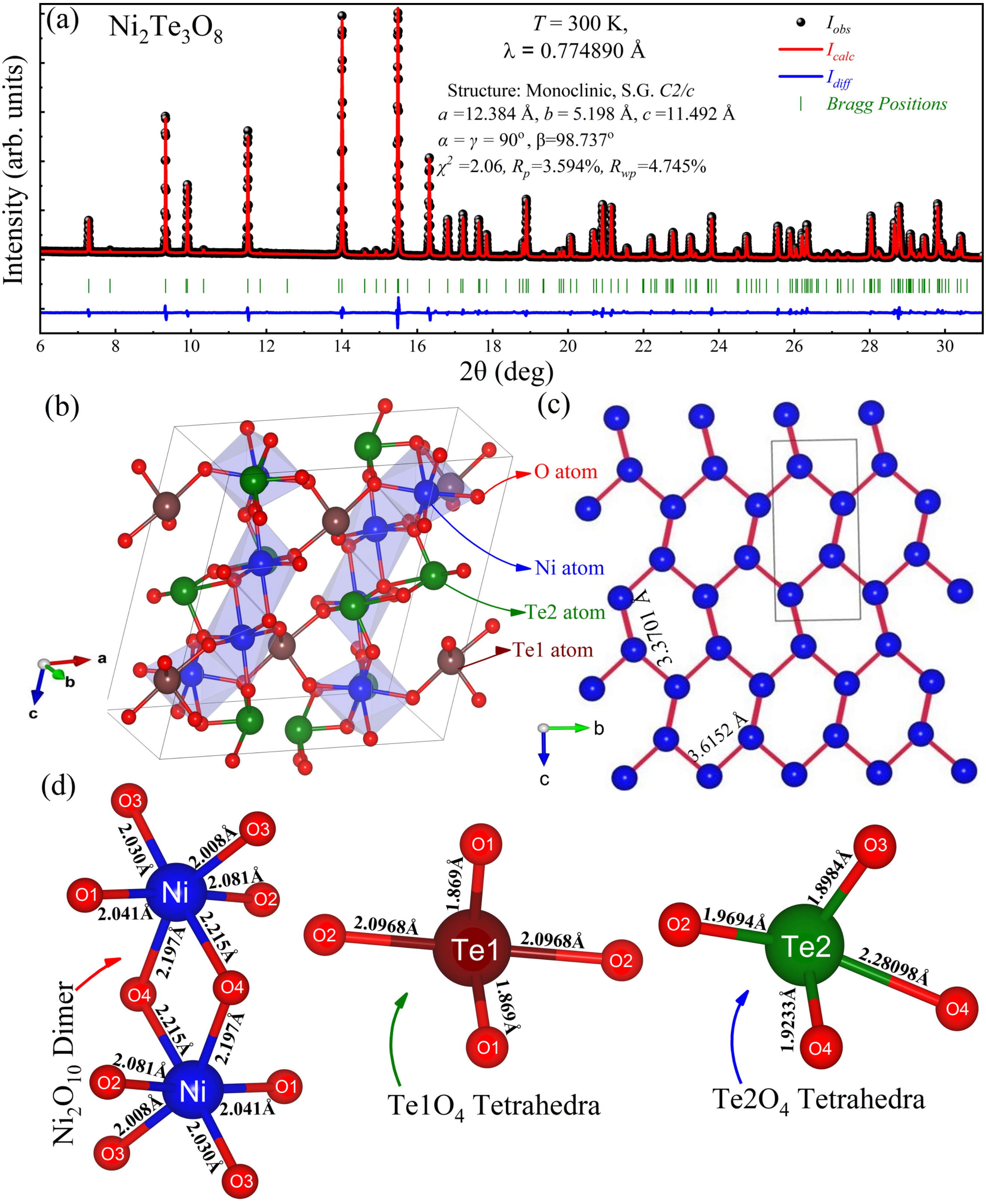

FIG. 1. (a) Rietveld refinement of high-resolution SXRD of powdered $Ni_2Te_3O_8$ at 300 K; (b) the crystal structure of $Ni_2Te_3O_8$ in which blue octahedra represent the Ni^{2+} in the zigzag c-axis direction with NiO_6 atomic arrangement and Te1 is shown in brown, Te2 is shown in green, and oxygen is in red. (c) Ni^{2+} atomic arrangement in the bc place with buckled honeycomb lattice. (d) Shows the bond lengths for Ni_2O_{10} dimers, $Te1O_4$, and $Te2O_4$ tetrahedra.

Material, Table S1 [37], consistent with a previously published report [30]. The crystal structure consists of 2D slabs (*bc* plane) composed of corner-shared $Te2^{4+}O_4$ coupled to the alternative corner and edge-shared $Ni^{2+}O_6$ octahedral. The $Te1^{4+}O_4$ act as buffer layers between the 2D slabs. The corner- and edge-sharing NiO_6 form the zigzag and buckled chains formed along the *c* axis, as shown in Fig. 1(b), and the layered buckled honeycomb configuration of Ni^{2+} in the *bc* plane, as shown in Fig. 1(c). From the crystallographic structure point of view, honeycomb layers consist of two distinct Ni^{2+} to Ni^{2+} bond lengths corresponding to bond-sharing (3.3701 Å) and edge-sharing (3.6152 Å) NiO_6 octahedra. The magnetic exchange interactions among Ni^{2+} ions occur via bond-shared oxygen atoms (Ni-O-Ni) within the *bc* plane. Furthermore, the bond lengths for Ni_2O_{10} dimers, and $Te1O_4$ and $Te2O_4$ tetrahedra at room temperature are also shown in Fig. 1(d).

B. Magnetic, specific heat, and dielectric properties

The *T* dependence of zero field cooled (ZFC) and field cooled (FC) magnetic susceptibility (χ) displays an archetypal three-dimensional (3D) long-range antiferromagnetic anomaly at $T_N \sim 35$ K [shown in Fig. 2(a)] despite having a 2D honeycomb Ni^{2+} lattice. The negative $\theta_{CW} \sim -79.204$ K from the experimental fit of the Curie-Weiss (CW) law $\chi = C/(T - \theta_{CW})$ denotes the dominant AFM interactions. The calculated μ_{eff} $[= \sqrt{3K_BC/N_A}] \sim 3.35\mu_B$ is slightly higher than the spin-only magnetic moment, which hints at the finite spin-orbit coupling and is consistent with several other Ni-based magnetic materials [39–41]. Furthermore, below T_N, *M* increases linearly with *H* and does not pertain to saturation even up to 7 T, demonstrating the absence of any possible metamagnetic/spin-flip transition up to 7 T (shown in Fig. S1 in the Supplemental Material [37]).

Specific heat (C_P vs *T*) with and without *H* is shown in Fig. 2(b). $C_P(T)$ demonstrates a peak with the sharp onset at $T_N \sim 35$ K. The λ-type transition in $C_P(T)$, as seen in the inset of Fig. 2(b), indicates a second-order phase transition occurring at T_N, particularly at low *T*. Along with χ vs *T*, the C_P vs *T* anomaly supports the long-range AFM order below T_N. Moreover, the inset of Fig. 2(b) demonstrates that neither the position nor the shape of the C_P vs *T* anomaly changes under external magnetic field (*H*) up to 7 T. These experimental results indicate the robustness of the AFM ground state in $Ni_2Te_3O_8$ compared to its sibling compounds Ni_3TeO_6 and $NiTe_2O_5$ [8,26,27,41].

Because the compound from $NiO-TeO_2$ exhibits exotic multiferroic and magnetoelectric properties, it is highly appealing to know the magnetoelectric properties of $Ni_2Te_3O_8$. The ε' vs *T* curve for $H = 0\,T$ in Fig. 2(c) illustrates the strong dielectric anomaly (T_D) near $T_N = 35$ K, which discloses magnetoelectric coupling. Furthermore, the ε' vs *H* curve at 20 K, with a negative magnetodielectric percentage (MD%) (∼ −0.0032%), confirms finite magnetoelectric coupling, shown in the inset of Fig. 2(c). Similar MD or multiferroic behaviors have been observed in several systems, such as $Cu_9O_2(SeO_3)_4Cl_6$, Pb_2MnO_4, and $CoTeMoO_6$ [42–44]. However, a comprehensive check for possible electrical polarization (*P*) (not shown) with and without *H* indicates the absence of a detectable pyrocurrent (I_{py}) signal (not shown here) within our experimental resolution, which rules out the possible spin-induced *P*.

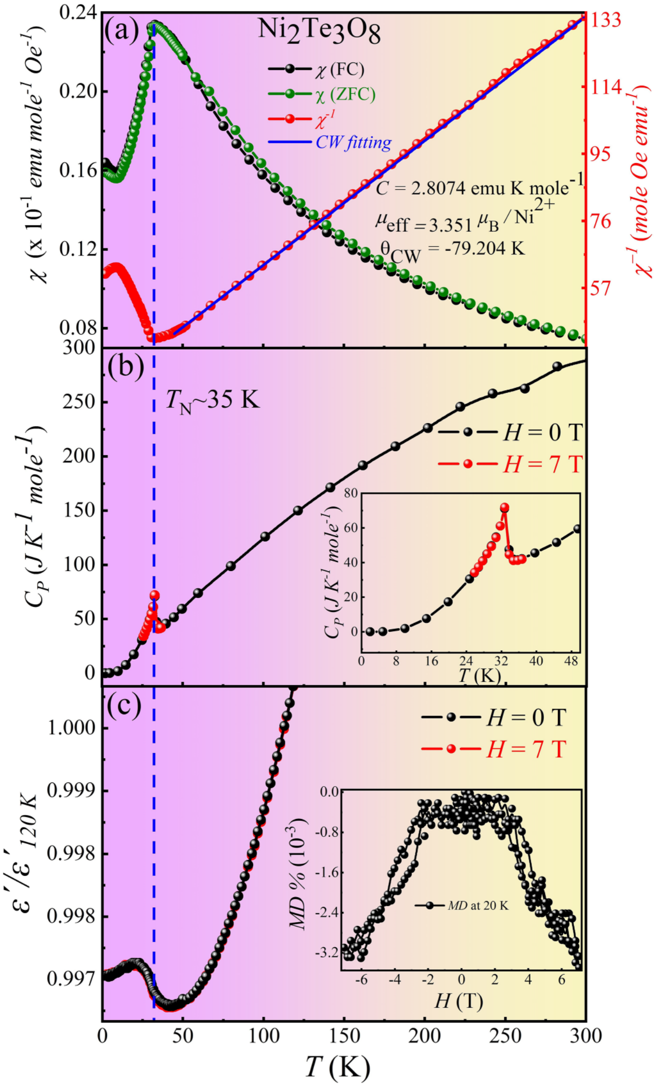

FIG. 2. (a) ZFC-FC susceptibility (right *y* axis) and inverse susceptibility (left *y* axis) of $Ni_2Te_3O_8$ at $H = 1000$ Oe; (b) C_P vs *T* curve in the *T* range 2–300 K under external $H = 0$ T and 7 T; inset shows the zoomed-in view of C_P vs *T* curves under *H* peaks at T_N appeared robust for *H* up to 7 T. (c) Shows ε' vs *T* at 1 MHz and 0 and 7 T fields with an apparent dielectric anomaly at T_N which is around 35 K, and MD% at 20 K and 1 MHz frequency is shown in inset; a clear correspondence between $\chi(T)$, $C_P(T)$, and $\varepsilon'(T)$ has been noticed.

C. Neutron diffraction for determining the T_N and spin structure

The neutron powder diffraction was utilized to gain insights into the type of magnetic ordering and spin arrangements that are in the hexagonal Ni network. To differentiate magnetic reflections from nuclear reflections, diffraction measurements were performed at 40 K (> T_N) and 3 K (< T_N), which are shown in Figs. 3(a) and 3(b). The NPD patterns were refined using monoclinic *C*2/*c* crystalline space groups

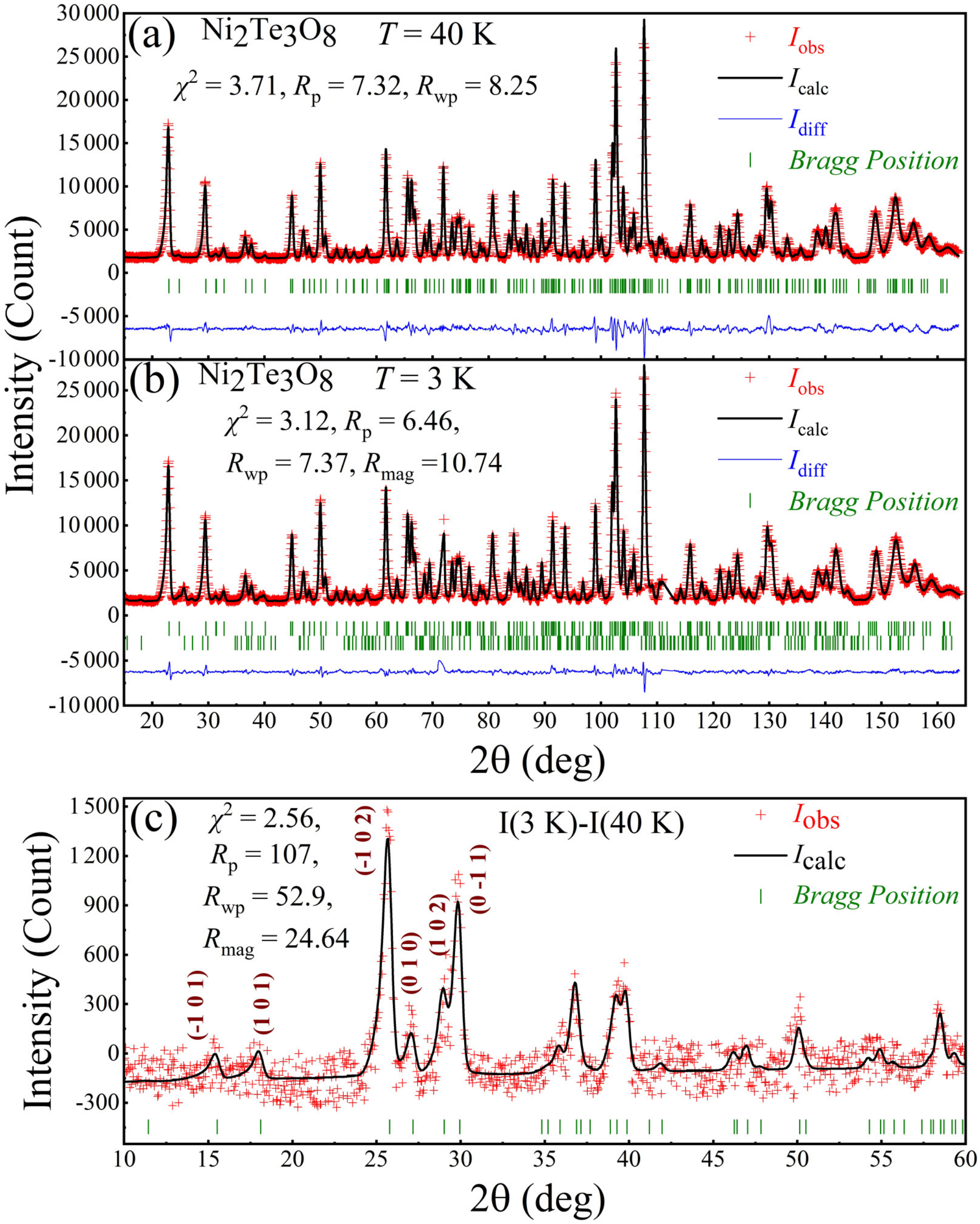

FIG. 3. Observed (crosses) and fitted (solid lines) neutron diffraction pattern at (a) 3 K and (b) 40 K, assuming a monoclinic C_P2'/c magnetic space group for the Ni spins. (c) The magnetic peaks below T_N and the refinement of neutron scattering. The solid green vertical lines represent the calculated Bragg reflections of the refined magnetic structure of $Ni_2Te_3O_8$. The incoherent magnetic scattering by the paramagnetic spins concentrates on the magnetic Bragg peaks below T_N, resulting in a negative background in the difference pattern.

down to the lowest T of 3 K [see Fig. 3(b)], and the structural parameters are summarized in Table S2 [37]. At 3 K, several additional Bragg peaks appear in the NPD pattern, which can be ascribed to the spin structure of the Ni hexagonal network. For the spin structure analysis, magnetic reflections were isolated by calculating the difference between the 3 and 40 K patterns [see Fig. 3(c)]. All magnetic reflections were indexed to a commensurate magnetic structure with a propagation vector $\mathbf{k} = (100)$. A symmetry analysis based on the BASIREPS program yielded four allowed irreducible representations, namely, Γ1, Γ2, Γ3, and Γ4, for the $C2/c$ space group coupled to the (100) propagation vector and their fittings are shown in Fig. S2 [37]. The different basis vectors calculated using the projection operator technique associated with each irreducible representation are presented in Table II. The best fit was achieved with the model described by the Γ3 representation with the magnetic space group C_P2'/c (OG #15.7.98) [45]. The final refinement for the difference of the 3–40 K NPD pattern is shown in Fig. 3(c) with fitting parameters $\chi^2 = 2.56$, $R_p = 107$, $R_{wp} = 52.9$, and $R_{mag} = 24.64$.

The spin arrangement obtained from fitting the 3 K magnetic pattern is depicted in Figs. 4(c) and 4(d). The Ni network forms 2D layers in the bc planes aligned along the crystallographic a axis. The Ni^{2+} spins on the honeycomb

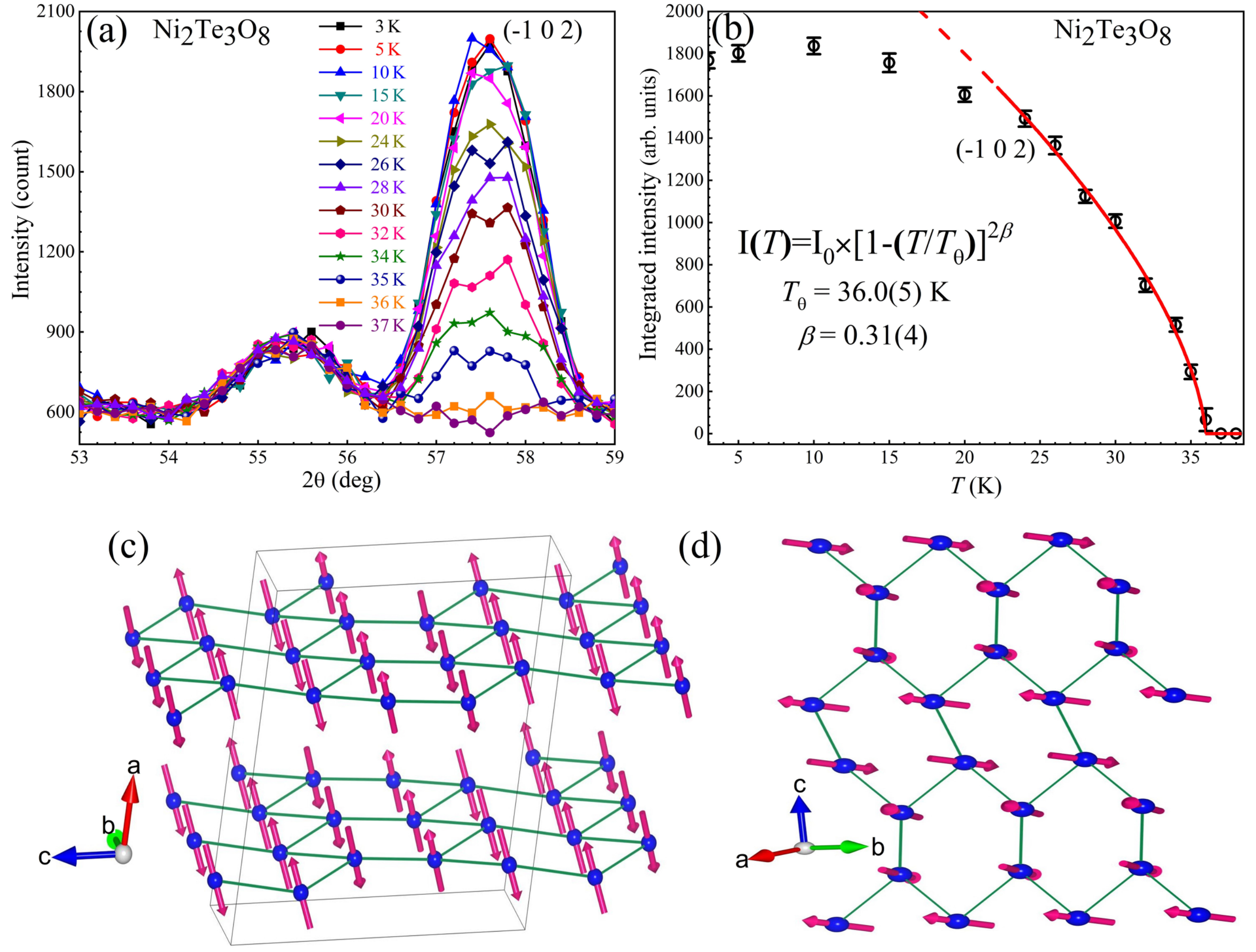

FIG. 4. (a,b) T dependence of the (-102)-q integrated intensities presenting an antiferromagnetic ordering $T_N = 35$ K for the Ni spin. The proposed Ni spin arrangements in $Ni_2Te_3O_8$: (c) antiferromagnetic stacking of Ni spin along the crystallographic a-axis direction in the half unit cell; (d) Ni spin configuration in the severely distorted buckled honeycomb layer in the bc plane.

lattice are essentially pointing out of the layers, and the major component of the spins are along the a axis. However, a canting angle of 23.75° causes the magnetic moments to deviate from the a axis, resulting in finite spin components in the bc plane. Table III presents the magnetic moments and their components along the three crystallographic axis directions. The magnetic interaction within the Ni layers occurs through both edge-shared Ni-Ni ($\angle$Ni$-$O$-$Ni $= 100.98^\circ$) and corner-shared Ni-Ni ($\angle$Ni$-$O$-$Ni $= 127.61^\circ$) arrangements, deviating from the 90° ferromagnetic superexchange interaction, resulting in an antiferromagnetic ground state with slightly canted moments away from the a axis. The refined total ordered magnetic moment at 2 K is $2.0098(5)\mu_B$, consistent with the theoretical spin-only ordered value for Ni^{2+}.

TABLE II. Irreducible representations for $C2/c$ (no. 15) space group with $\mathbf{k} = (100)$ in terms of the Bertaut's notations, $F(++++)$, $C(+-+-)$, $G(++--)$, and $A(+--+)$. The basis vectors are assigned to the sites: (i) (x, y, z), (ii) $(-x, y, -z + 1/2)$, (iii) $(-x, -y, -z)$, and (iv) $(x, -y, z + 1/2)$. The spins generated by the C-center translation (1/2, 1/2, 0) are antiparallel. Four models are tested one by one, and the magnetic R factors obtained for Γ1, Γ2, Γ3, and Γ4 are 18.84, 27.77, 10.71, and 27.90, respectively.

Ireps.	Γ1	Γ2	Γ3	Γ4
	$G_xF_yG_z$	$A_xC_yA_z$	$F_xG_yF_z$	$C_xA_yC_z$
x, y, z	U, V, W	U, V, W	U, V, W	U, V, W
$-x, y, -z + \frac{1}{2}$	$-U, V, -W$	$-U, V, -W$	$U, -V, W$	$U, -V, W$
$-x, -y, -z$	U, V, W	$-U, -V, -W$	U, V, W	$-U, -V, -W$
$x, -y, z + \frac{1}{2}$	$-U, V, -W$	$U, -V, W$	$U, -V, W$	$-U, V, -W$

The precise antiferromagnetic transition T_N was determined by tracing the thermal variation of the strong magnetic reflection peak (-102) at different temperatures, as shown in Fig. 4(a). The intensity $I(T)$ vs T, as shown in Fig. 4(b), was fitted with power law $I = I_0\{(1–T/T_N)\}^{2\beta}$ [solid curve in Fig. 4(b)], where I_0 denotes the saturation magnetic intensity and β is the critical exponent of the magnetic transition. This result is corroborated with the (T) and $C_P(T)$ data shown in Figs. 2(a) and 2(b). The obtained critical exponent $\beta = 0.31(4)$ is larger than those obtained in the 2D Ising ($\frac{1}{8}$) or 2D XY (0.25) models. However, it was close to the 3D Ising of $\beta = 0.33$ or 3D Heisenberg of $\beta = 0.36$, which further

TABLE III. Ni^{2+} magnetic moment components along three crystallographic axis directions and the canting angle with an *a* axis.

m_x	m_y	m_z	$m = \sqrt{m_x^2 + m_y^2 + m_z^2}$	Angle between the spin and *a* axis (deg)
−1.7028	−0.5750	−0.8997	2.009878	156.2752
−1.7028	−0.5750	−0.8997	2.009878	23.72479

supports the established archetypical three-dimensional AFM order of the DC magnetization and hints at the finite magnetic exchange-correlation present between the 2D honeycomb layers [46,47].

D. *T*-dependent SXRD: Magnetoelastic effect

To elucidate the origin of the dielectric and MD behavior, *T*-dependent XRD of $Ni_2Te_3O_8$ was performed in the *T* window of 300–20 K; all SXRD patterns are shown in Figs. S3(a) and S3(b) [37]. From the XRD reflection along with Rietveld refinement at 20 and 115 K [shown in Figs. 5(a) and 5(b)],

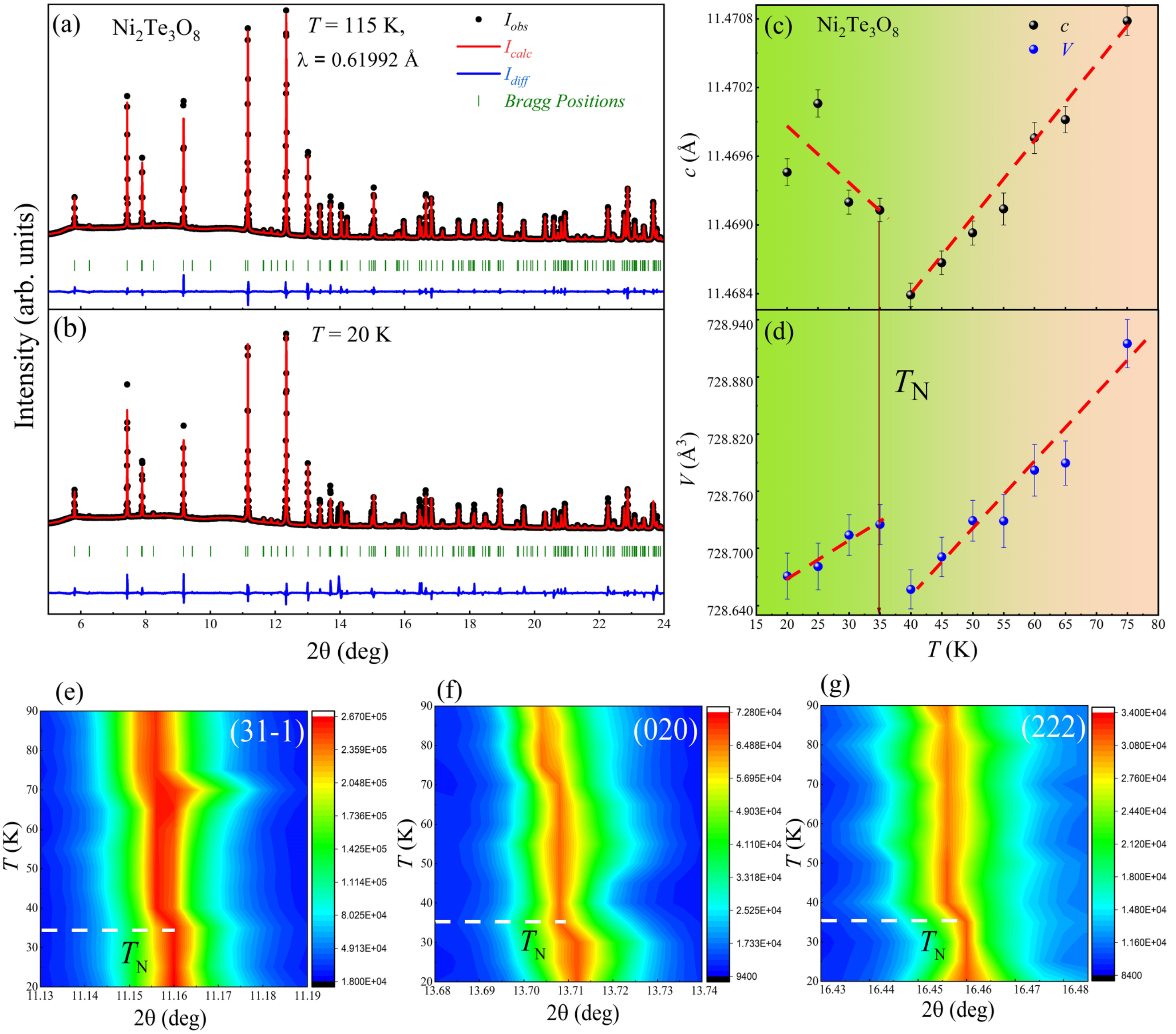

FIG. 5. (a,b) *T*-dependent high-resolution SXRD pattern with Rietveld refinement of $Ni_2Te_3O_8$ powdered sample at (a) 20 K and (b) 115 K. (c,d) *T* variation of the lattice parameters *c* and unit cell volume (*V*); dashed lines (red) represent a guide to the eye; clear discontinuity has been noticed at T_N. (e–g) show the 3D contour plots to reflect the changes in the lattice parameters near the T_N in multiple reflections such as (31-1), (020), and (222).

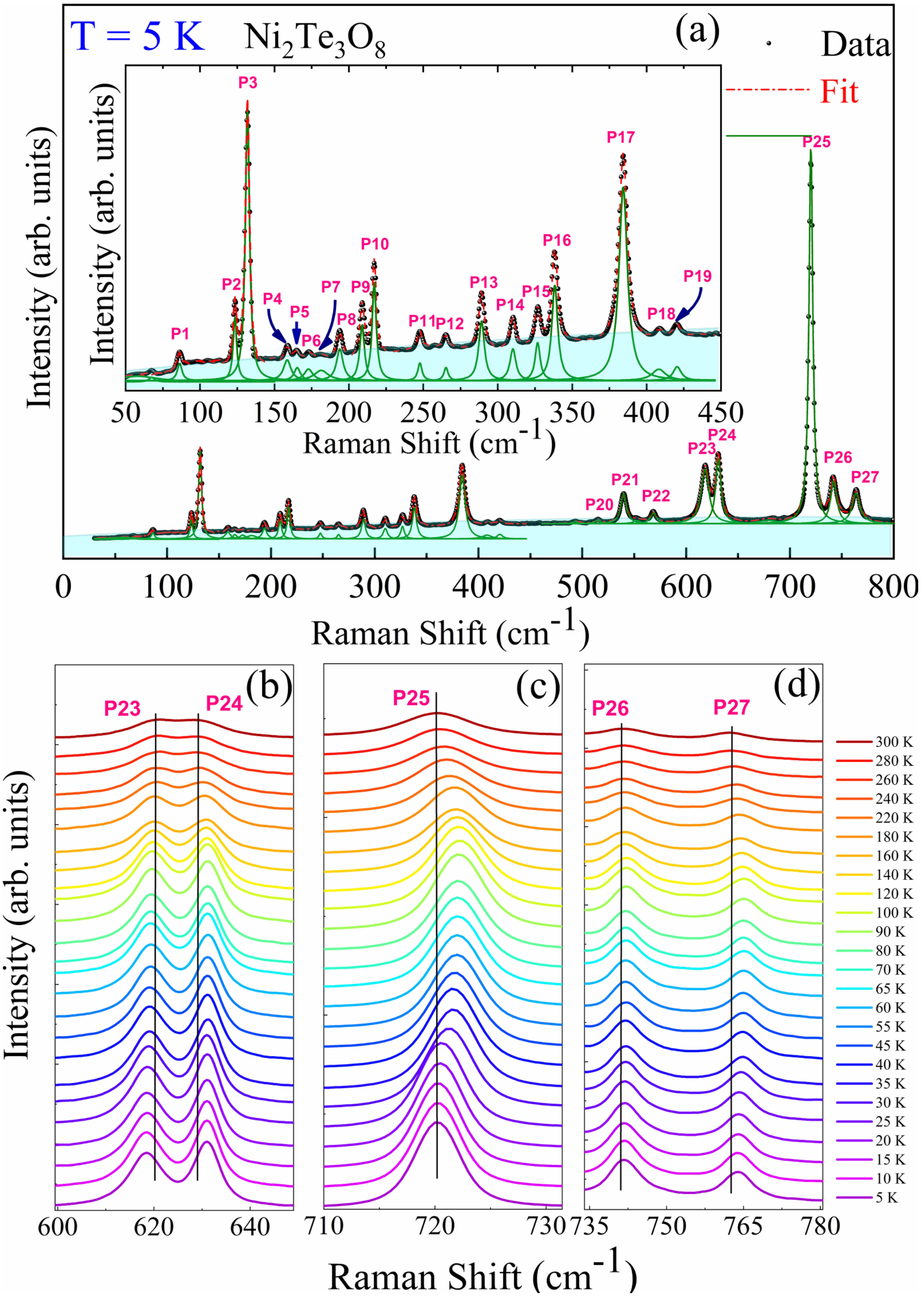

FIG. 6. (a) Raman scattering spectrum of Ni$_2$Te$_3$O$_8$ collected at 5 K. Using the Lorentzian model, the dashed line and solid lines denote the optimal fit and individual peaks. The shaded area represents a broad background in the spectrum; (b–d) T-dependent selected Raman modes (P23–P27) for Ni$_2$Te$_3$O$_8$; the solid black line illustrates a guide to the eye for Raman mode changes (hardening or softening).

it was clear that the monoclinic $C2/c$ crystalline symmetry was preserved without any global structural transformation from 115 to 20 K. However, the SXRD intensity color contour figures for the selected Bragg's reflections (31-1), (020), and (222) [Figs. 5(e)–5(g)] portray a notable change near T_N; it is evident the local structural changes occur near T_N. To evaluate the local structural changes (lattice parameters and bond lengths), the T-dependent c-lattice parameter and unit cell volume are presented in Figs. 5(c) and 5(d). As expected, all the lattice parameters in Fig. 5 and Fig. S4 [37], including the unit cell volume, decreased with T. However, a detailed analysis of the lattice parameters shows anomalies near T_N, where a slope change appeared in the positive thermal expansion. This result indicates that the elastic changes at the onset of T_N signify magnetoelastic coupling that collaborates with the changes in the lattice dielectric constant [44,48–50]. Furthermore, a detailed analysis of bond lengths and angles for all atoms directs attention to the visible anomalies occurring near 100 K and T_N (shown in Figs. 8(a) and 8(b) as well as Figs. S4–S6 [37]); this suggests the finite local structural relaxation happening at 100 K is further amplified by the magnetic ordering of Ni atoms.

E. Raman spectroscopy and spin-phonon coupling

To better understand the magnetoelastic coupling and explore the possible correlation between the phonon and magnetic degrees of freedom, we performed Raman spectroscopy measurements over a wide T range (5–300 K). According to the results of factor group analysis, $Ni_2Te_3O_8$ has a monoclinic structure (space group $C2/c$: No. 15) with four formula units per crystallographic unit cell. The primitive unit cell has two formula units and, therefore, 26 atoms, resulting in 78 phonons (75 optical and three acoustic) [28]. The irreducible representation of the phonon modes at the center of the Brillouin zone is given by $\Gamma = 19A_g + 20B_g + 19A_u + 20B_u$ [45]. A total of 39 modes were Raman active, comprising $19A_g + 20B_g$. The 36 modes $(18A_u + 18B_u)$ are infrared active, while the three modes $(A_u + 2B_u)$ are acoustic. Figure 6(a) shows the Raman scattering spectrum of $Ni_2Te_3O_8$ collected at 5 K, and the complete Raman spectrum from 300 to 5 K is shown in Fig. S7 [37]. The spectrum is composed of 27 phonon modes and a broad photoluminescence background. We fitted the phonon peaks using Lorentzian functions. Phonon mode assignments have been performed by comparing the Raman spectrum of the isostructural $Co_2Te_3O_8$ compound as reported in Ref. [29]. The symmetric stretching vibration of $(Te_2O_5)^{2-}$ and the Te-O antisymmetric stretching vibration have been assigned to the strong intensity peaks observed at 720 cm^{-1} (P25) and 630 cm^{-1} (P24), respectively. Additionally, the Te-O bending vibrations are attributed to the bands observed at 336 cm^{-1} (P16) and 380 cm^{-1} (P17). Furthermore, the results obtained from the theoretical phonon density of states (as shown in Fig. S12(a) [37]) partially support the aforementioned mode assignments. Specifically, the atomic vibrations responsible for the prominent Raman mode (P25) are more complex and involve stretching/antistretching vibrations of Te_2O_3, coupled with bending/stretching vibrations of Ni-O(1,2,3,4) atoms (shown in Fig. S12(b) [37]).

The T-dependent Raman scattering spectra of $Ni_2Te_3O_8$ for specific modes with prominent changes such as P23, P24, P25, P26, and P27 are shown in Figs. 6(b)–6(d). The spectra at each temperature were analyzed using the Lorentzian function to extract the phonon parameters. Modes P1, P19, and P20 are weak; therefore, their T dependence cannot be extracted. Figure 7 and Figs. S8–S10 [37] illustrate the frequencies and linewidths of the phonon modes as a function of temperature. Most phonon modes exhibit an anharmonic trend with T (i.e., decreasing frequency and increasing linewidth with increasing temperature), arising from thermal expansion and lattice anharmonicity. Notably, the P23 (620 cm^{-1}) mode presents a blueshift with an increase in T over the investigated T range (5–300 K). This peculiar behavior of the P23 mode might be associated with strong anharmonic phonon-phonon interactions in the $Ni_2Te_3O_8$ lattice and merits further investigation [51–55]. In general, according to the anharmonic model, the phonon frequency as a function of T due to cubic anharmonicity can be written as follows [18,56–59]:

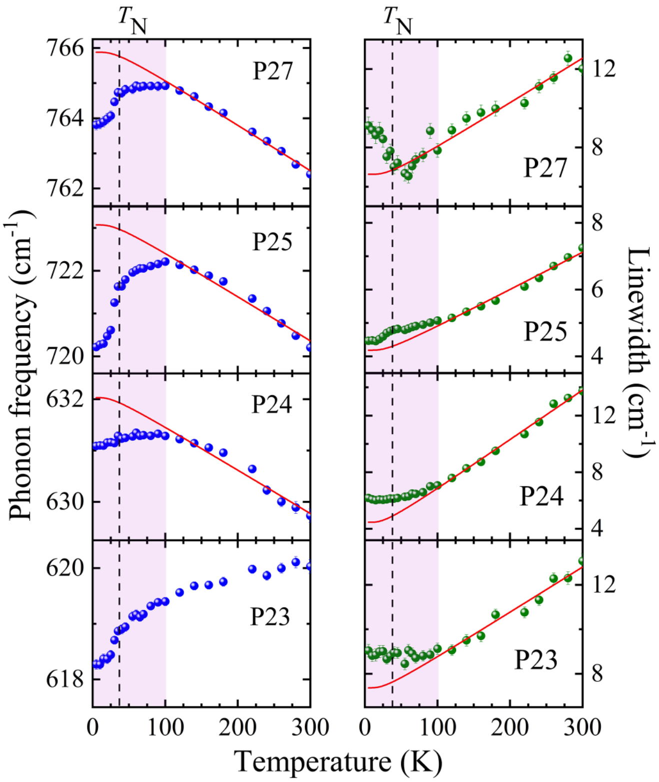

FIG. 7. Phonon frequency/linewidth vs T for intense modes. The thin solid lines are the fitting results of the anharmonic model [Eqs. (1) and (2)]. The pink zone for $T < 100$ K indicates the deviation of Raman modes from the anharmonic trend, and the vertical dashed line denotes T_N at 35 K.

$$\omega_{\text{anh}}(T) = \omega_0 + A\left[1 + \frac{2}{\left(e^{\frac{\hbar\omega_0}{2k_B T}} - 1\right)}\right]. \tag{1}$$

Similarly, the temperature-dependent phonon linewidth due to cubic anharmonicity can be expressed as follows:

$$\Gamma_{\text{anh}}(T) = \Gamma_0 + C\left[1 + \frac{2}{\left(e^{\frac{\hbar\omega_0}{2k_B T}} - 1\right)}\right], \tag{2}$$

where ω_0 and Γ_0 are the frequency and linewidth of a phonon at zero temperature, respectively. A and C are the cubic anharmonic coefficients of the frequency and linewidth, respectively. $\hbar$ is the reduced Planck constant, k_B is the Boltzmann constant, and T is the variable temperature. The T-dependent phonon frequency and linewidth were analyzed using Eqs. (1) and (2), and the best-fitting parameters are listed in Table S3 [37]. All modes exhibit a deviation in their parameters (frequency and linewidth) from an anharmonic trend at low temperatures (Fig. 7 and Figs. S8–S10 [37]). Notably, most of these phonon anomalies start appearing at approximately 100 K, well above the magnetic phase transition T ($T_N \sim 35$ K), which will be further discussed. In

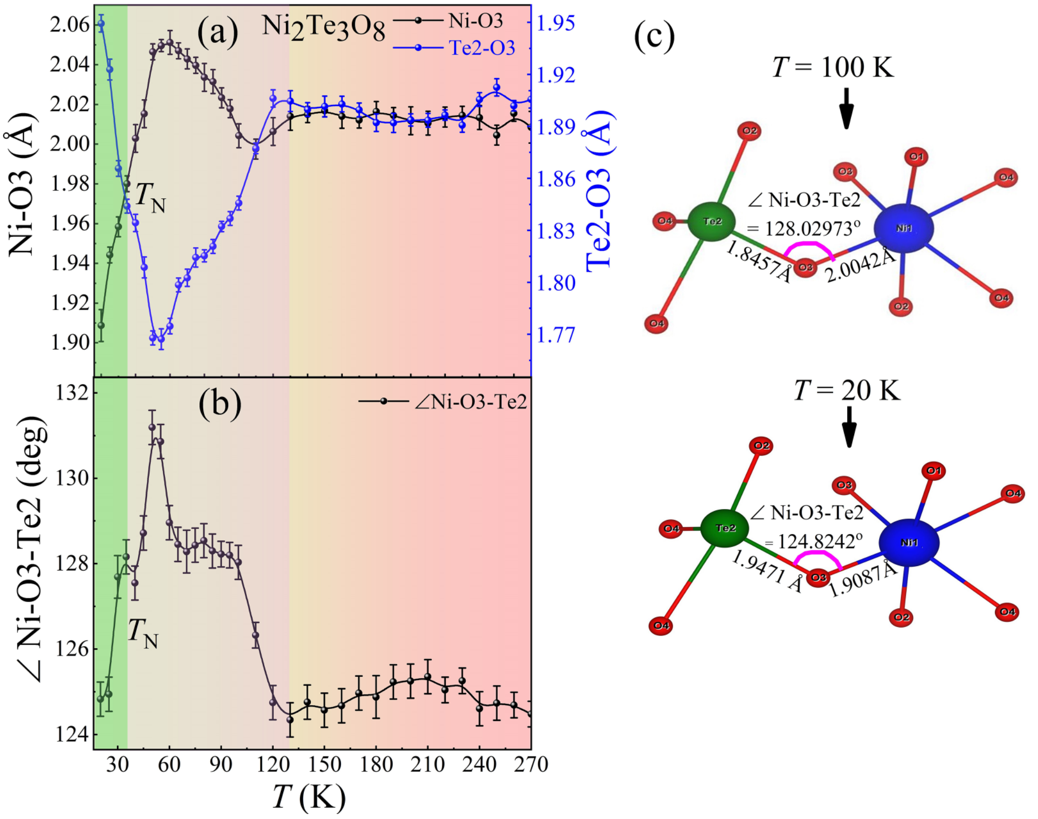

FIG. 8. (a) shows the thermal variation in the bond length of Ni-O3 and Te2-O3 and (b) shows the T-dependence variation of bond angle ∠Ni-O3-Te2, representing the evident distortion near T_N. (c) shows the pictorial representation of bond length and bond angle from Ni-O3-Te2.

addition, the frequencies of the P8, P21, P25, P26, and P27 modes showed a change in slope (ω vs T) at T_N. In magnetic materials, the temperature-dependent frequency change in the phonon mode can be written as follows [58,59]:

$$\Delta\omega(T) = \Delta\omega_{\text{qh}} + \Delta\omega_{\text{anh}} + \Delta\omega_{\text{SPC}} + \Delta\omega_{\text{EPC}}, \qquad (3)$$

where $\Delta\omega_{\text{qh}}$ represents the quasiharmonic contribution arising solely from the thermal expansion of the lattice. The change in frequency owing to intrinsic anharmonicity is given by $\Delta\omega_{\text{anh}}$. $\Delta\omega_{\text{SPC}}$ and $\Delta\omega_{\text{EPC}}$ are the spin-phonon and electron-phonon coupling terms, respectively. Owing to the insulating nature of $Ni_2Te_3O_8$, the role of electron-phonon coupling can be safely ruled out. Bulk magnetization and neutron diffraction measurements did not indicate spin-spin correlations or short-range magnetic ordering above $T_N(\sim 35\,\text{K})$. Moreover, T-dependent x-ray diffraction measurements did not reveal any global structural phase transitions in the $Ni_2Te_3O_8$ down to 20 K (Fig. 5). Evidently, local structure parameters such as bond lengths and angles exhibit a noticeable change as shown in Figs. 5, 8(a), and 8(b), and Figs. S5 and S6 [37]. A substantial variation in the bond lengths of Te atoms in $Te2_2O_6$ near 100 K (Figs. 8(a) and 8(b) and Figs. S5 and S6 [37]) might be the possible source for the deviation of anharmonic fits. Further, the unit cell volume (V), Ni-O3-Te2 bond length, and ∠Ni-O3-Te2 angle all showed a change in slope at T_N, which implies visible magnetoelastic coupling happens via changes in the local bond lengths of the $Ni_2Te_3O_8$ lattice. The softening of the phonon modes of $Ni_2Te_3O_8$ at the magnetic phase transition T suggests that the onset of magnetic ordering alters the atomic displacement characteristics. In general, for magnetic oxides, the deviation of the phonon mode from the anharmonic model is ascribed by considering the spin-spin correlation function [60,61].

$$\Delta\omega_{\text{SPC}} = \omega - \omega_0 = \lambda_{\text{sp-ph}}\,\langle S_i S_j\rangle, \qquad (4)$$

where ω is the renormalized phonon frequency due to spin-phonon coupling, ω_0 is the phonon frequency in the absence of this coupling $\langle S_i S_j\rangle$ denote a statistical average of the spin-pair correlation function, and $\lambda_{\text{sp-ph}}$ is the spin-phonon coupling constant. Under the mean-field approximation (i.e., $\langle S_i S_j\rangle = \langle S_i\rangle\langle S_j\rangle$), the spin-spin correlation function $\langle S_i S_j\rangle$ can be related to static magnetization through the equation $\Delta\omega_{\text{SPC}} \approx \mathbf{M}^2(T)$; where $\mathbf{M}(T)$ represents the magnetization of the sample at temperature T [62–64]. By following this approach, we can estimate the spin-phonon coupling constant, i.e., $\Delta\omega_{\text{SPC}} = \lambda_{\text{sp-ph}}\langle S_i S_j\rangle \;= 3[\mathbf{M}^2(T)/\mathbf{M}^2_{\text{max}}]$, where the factor of 3 accounts for the nearest neighbor Ni atoms [62]. As demonstrated in both Fig. 9(a) and Figs. S11(a)–S11(c) [37], at least four Raman modes (P2 and P25–P27) exhibit a strong correlation and follow a similar variation below T_N. The linear fit of $\Delta\omega$ vs $\mathbf{M}^2(T)/\mathbf{M}^2_{\text{max}}$ has been used to estimate the spin-phonon coupling constant $\lambda_{\text{sp-ph}}$ and is shown in Fig. 9(b), Figs. S11(d)–S11(f), and Table S4 [37]. A similar approach has been employed to estimate the $\lambda_{\text{sp-ph}}$ values in many magnetic oxide systems [62,65–68]. Notably, the obtained $\lambda_{\text{sp-ph}}$ values were moderate and were found to be comparable to those reported for several established multiferroic systems, such as $9R-BaMnO_3$, $15R-BaMnO_3$, CuB_2O_4,

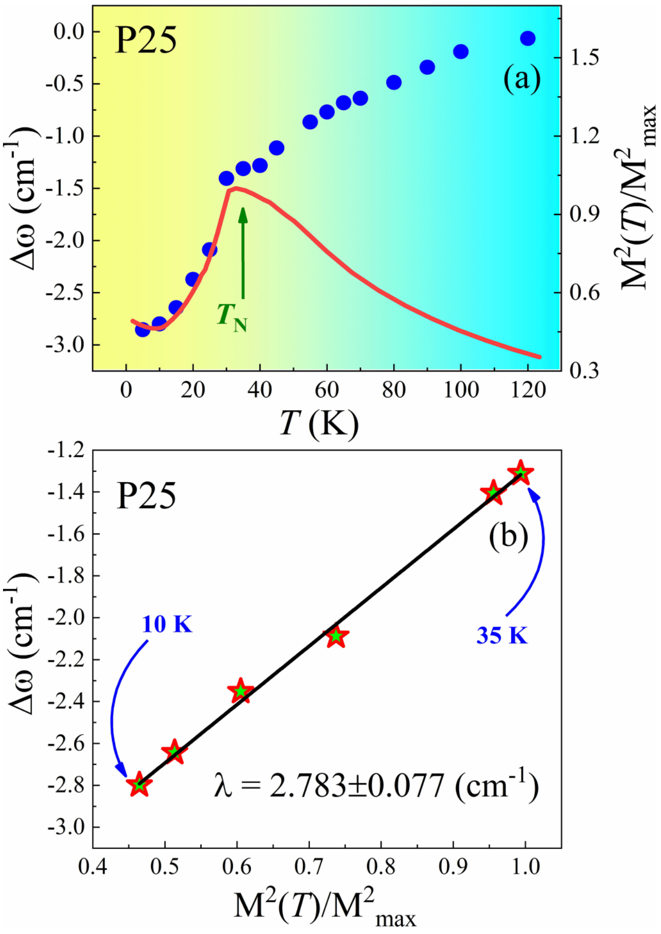

FIG. 9. (a) T-dependence variation of $\Delta\omega$ vs T (left) and $\mathbf{M}^2(T)/\mathbf{M}^2_{\rm max}$ vs T (right) for P25 phonon mode, which corresponds to the spin-phonon coupling below $T_{\rm N}$. (b) shows $\Delta\omega$ vs $\mathbf{M}^2(T)/\mathbf{M}^2_{\rm max}$ for the intense phonon mode P25 and its linear fitting to evaluate the spin-phonon coupling constant λ.

$ZnCr_2O_4$, $GaFeO_3$ $NdBaMn_2O_5$, etc. [36,37,61,67,69–71], and other magnetic compounds [72–76]. However, $\lambda_{\rm sp-ph}$ values were much smaller than NiO, CuO, and $NaOsO_3$ [77–79]. The relatively large λ values of the P25 modes suggest that the stretching vibrations of the Te2-O-Ni bond network play a crucial role in the spin-phonon coupling observed in $Ni_2Te_3O_8$, where the spin-phonon coupling arises from the modulation of the superexchange interaction due to the ionic movement of the Te2-O-Ni bonds. In magnetoelectric systems, the presence of spin-phonon coupling, the phonon ω effect by the q-dependent spin-spin correlations, results in modification of permittivity via the Lyddane-Sachs-Teller equation. $\varepsilon_0 = \frac{\omega_{\rm L}^2}{\omega_{\rm T}^2}\,\varepsilon_\infty$, where ε_0 and ε_∞ are the permittivity at zero frequency and optical frequency, respectively, and $\omega_{\rm L}^2$ and $\omega_{\rm T}^2$ are the long-wavelength longitudinal and transverse optical phonon modes [80]. A similar spin phonon induced dielectric anomaly has been noticed in several $CoTiO_3$, $NiTiO_3$, $Se/TeCuO_3$, $CoCr_2O_4$, and $CoTeMoO_6$ [43,81–84] magnetoelectric systems.

F. Comparison between Ni_3TeO_6, $NiTe_2O_5$, and $Ni_2Te_3O_8$

It is inspiring to compare the compounds' crystal structures and physical properties from the NiO−TeO_2 binary phase diagram. Based on the oxidation state and chemical environment, Te lone-pair ions act as a chemical that effectively terminates the crystal growth and leads to a low-dimensional crystal lattice [24], as shown in Table I and Table S5 [37]; lone-pair ions drive the asymmetric coordination geometry of $Te^{4+}O_3/Te^{4+}O_5$ in $NiTe_2O_5$ and $Te^{4+}O_4$ in $Ni_2Te_3O_8$. This leads to low-dimensional Ni^{2+} lattices for $NiTe_2O_5$ (quasi-one-dimensional Ni^{2+} spin chains) and $Ni_2Te_3O_8$ (and a two-dimensional honeycomb lattice). In contrast, $Te^{6+}O_6$ is not a lone-pair ion in Ni_3TeO_6, leading to the 3D connection of Ni^{2+} atoms in the crystal lattice. Despite having the Te stereochemically active lone pair of electrons, $NiTe_2O_5$ and $Ni_2Te_3O_8$ compounds fall into the centrosymmetric class. Apart from the diverse crystal structures, the physical properties of the NiO−TeO_3 phase diagram are exciting. Polar Ni_3TeO_6 shows a giant spin-induced electrical polarization at $T_{\rm N} = 55$ K due to the collinear ↑↑↓↓↑↑ exchange striction along the c-axis spin chain [25]. Furthermore, below $T_{\rm N}$, a successive metamagnetic and colossal magnetoelectric effect has been reported in Ni_3TeO_6 [85]. In contrast, the low-dimensional compounds $NiTe_2O_5$ and $Ni_2Te_3O_8$ did not generate electrical polarization despite having Te^{4+} lone-pair ions. However, complex magnetic behavior along with spin-charge-lattice coupling induced dielectric anomaly, and finite magnetoelectric coupling was observed below $T_{\rm N}$ for $NiTe_2O_5$ [8]. The present study investigated the crucial role played by the Ni-O3-Te2 bond in achieving intricate coupling of the spin-charge-lattice degrees of freedom in $Ni_2Te_3O_8$.

IV. CONCLUSION

In summary, the layered two-dimensional honeycomb magnetic lattice $Ni_2Te_3O_8$ was successfully synthesized and comprehensively studied: (1) The long-range antiferromagnetic ordering accompanied by a dielectric anomaly occurring at $T_{\rm N} \sim 35$ K with the presence of weak magnetodielectricity demonstrates the spin-charge coupling. (2) The ground-state antiferromagnetic layered honeycomb spin structure of $Ni_2Te_3O_8$ was determined by neutron diffraction. (3) Low-T spin-phonon coupling near magnetic ordering via Raman scattering, dielectric anomaly near $T_{\rm N}$, and a structural anomaly in T-dependent SXRD indicate the intricate interactions of spin-phonon-charge degrees of freedom in 2D layered honeycomb magnetic lattice $Ni_2Te_3O_8$.

ACKNOWLEDGMENTS

This study was supported by the Ministry of Science and Technology, Taiwan, under Grants No. MOST 110-2112-M-110-008-MY3, No. MOST 111-2811-M-110-010, No. MOST 112-2923-M-110-001, No. MOST 111-2112-M-110-017, No. MOST 111-2811-M-110-012, No. MOST 112-2112-M-110-018 and No. MOST 111-2112-M-003-016. The author J.-Y.L. is grateful to Y.-J. Hu for his help in the measurement of specific heat.

The authors declare no conflict of interest.

[1] A. Vasiliev, O. Volkova, E. Zvereva, and M. Markina, npj Quantum Mater. **3**, 18 (2018).
[2] A. P. Ramirez, Annu. Rev. Mater. Res. **24**, 453 (1994).
[3] N. A. Spaldin and R. Ramesh, Nat. Mater **18**, 203 (2019).
[4] D. C. Cabra, A. O. Dobry, C. J. Gazza, and G. L. Rossini, Phys. Rev. B **103**, 144421 (2021).
[5] D. C. Kakarla, Z. H. Yang, H. C. Wu, T. W. Kuo, A. Tiwari, W. H. Li, C. H. Lee, Y. Y. Wang, J. Y. Lin, C. K. Chang, B. H. Chen, C.-W. Wang, C. A. Lee, M. M. C. Chou, and H. D. Yang, Mater. Adv. **2**, 7939 (2021).
[6] S. Kimura, K. Kakihata, Y. Sawada, K. Watanabe, M. Matsumoto, M. Hagiwara, and H. Tanaka, Nat. Commun **7**, 12822 (2016).
[7] S. Seki, T. Kurumaji, S. Ishiwata, H. Matsui, H. Murakawa, Y. Tokunaga, Y. Kaneko, T. Hasegawa, and Y. Tokura, Phys. Rev. B **82**, 064424 (2010).
[8] A. Tiwari, D. C. Kakarla, G. Macam, C. H. Hsu, F. C. Chuang, H. C. Wu, T. W. Kuo, A. Pal, H. Chou, D. P. Gulo, H. L. Liu, Y. C. Chuang, Y. C. Lai, C. A. Lee, M. M. C. Chou, and H. D. Yang, Phys. Rev. Mater. **6**, 044409 (2022).
[9] V. Zapf, M. Jaime, and C. D. Batista, Rev. Mod. Phys. **86**, 563 (2014).
[10] W. J. L. Buyers, R. M. Morra, R. L. Armstrong, M. J. Hogan, P. Gerlach, and K. Hirakawa, Phys. Rev. Lett. **56**, 371 (1986).
[11] A. Banerjee, C. A. Bridges, J. Q. Yan, A. A. Aczel, L. Li, M. B. Stone, G. E. Granroth, M. D. Lumsden, Y. Yiu, J. Knolle, S. Bhattacharjee, D. L. Kovrizhin, R. Moessner, D. A. Tennant, D. G. Mandrus, and S. E. Nagler, Nat. Mater. **15**, 733 (2016).
[12] H. B. Cao, A. Banerjee, J. Q. Yan, C. A. Bridges, M. D. Lumsden, D. G. Mandrus, D. A. Tennant, B. C. Chakoumakos, and S. E. Nagler, Phys. Rev. B **93**, 134423 (2016).
[13] S. Choi, S. Manni, J. Singleton, C. V. Topping, T. Lancaster, S. J. Blundell, D. T. Adroja, V. Zapf, P. Gegenwart, and R. Coldea, Phys. Rev. B **99**, 054426 (2019).
[14] H.-S. Kim, V. Shankar V., A. Catuneanu, and H.-Y. Kee, Phys. Rev. B **91**, 241110 (2015).
[15] A. Kitaev, Ann. Phys. **321**, 2 (2006).
[16] H. Liu and G. Khaliullin, Phys. Rev. B **97**, 014407 (2018).
[17] Y. Motome, R. Sano, S. Jang, Y. Sugita, and Y. Kato, J. Phys.: Condens. Matter **32**, 404001 (2020).
[18] S. Mukherjee, G. Manna, P. Saha, S. Majumdar, and S. Giri, Phys. Rev. Mater. **6**, 054407 (2022).
[19] R. Sano, Y. Kato, and Y. Motome, Phys. Rev. B **97**, 014408 (2018).
[20] A. Scheie, K. Ross, P. P. Stavropoulos, E. Seibel, J. A. Rodriguez-Rivera, J. A. Tang, Y. Li, H.-Y. Kee, R. J. Cava, and C. Broholm, Phys. Rev. B **100**, 214421 (2019).
[21] Y. Singh, S. Manni, J. Reuther, T. Berlijn, R. Thomale, W. Ku, S. Trebst, and P. Gegenwart, Phys. Rev. Lett. **108**, 127203 (2012).
[22] H. K. Vivanco, B. A. Trump, C. M. Brown, and T. M. McQueen, Phys. Rev. B **102**, 224411 (2020).
[23] S. C. Williams, R. D. Johnson, F. Freund, S. Choi, A. Jesche, I. Kimchi, S. Manni, A. Bombardi, P. Manuel, P. Gegenwart, and R. Coldea, Phys. Rev. B **93**, 195158 (2016).
[24] A. G. Christy, S. J. Mills, and A. R. Kampf, Mineral. Mag. **80**, 415 (2016).
[25] Y. S. Oh, S. Artyukhin, J. J. Yang, V. Zapf, J. W. Kim, D. Vanderbilt, and S.-W. Cheong, Nat. Commun **5**, 3201 (2014).
[26] J. H. Lee, M. Kratochvílová, H. Cao, Z. Yamani, J. S. Kim, J.-G. Park, G. R. Stewart, and Y. S. Oh, Phys. Rev. B **100**, 144441 (2019).
[27] S.-H. Baek, J. H. Lee, Y. S. Oh, K.-Y. Choi, and B. Büchner, Phys. Rev. B **104**, 214431 (2021).
[28] C. R. Feger, G. L. Schimek, and J. W. Kolis, J. Solid State Chem. **143**, 246 (1999).
[29] N. Li, B. Manoun, Y. Tamraoui, Q. Zhang, H. Dong, Y. Xiao, P. Chow, P. Lazor, X. Lü, and Y. Wang, Phys. Rev. B **99**, 245125 (2019).
[30] R. Dawar, R. Babu, K. Ananthasivan, and S. Anthonysamy, J. Nucl. Mater. **493**, 219 (2017).
[31] T. Roisnel and J. Rodriguez-Carvajala, A windows tool for powder diffraction patterns analysis Materials Science Forum, in *Proceedings of the Seventh European Powder Diffraction Conference (EPDIC 7)*, edited by R. Delhez and E. J. Mittenmeijer (Trans Tech Publications Ltd., Switzerland, 2000), pp. 118–123.
[32] K. Momma and F. Izumi, J. Appl. Crystallogr. **44**, 1272 (2011).
[33] M. Avdeev and J. R. Hester, J. Appl. Crystallogr. **51**, 1597 (2018).
[34] C. M. Wu, G. Deng, J. S. Gardner, P. Vorderwisch, W. H. Li, S. Yano, J. C. Peng, and E. Imamovic, J. Instrum. **11**, P10009 (2016).
[35] S. Yano, G. N. Iles, J. C. Peng, and C. M. Wu, J. Surf. Investig.: X-Ray, Synchrotron Neutron Tech. **14**, S207 (2020).
[36] R. D. Mero, C.-H. Lai, C.-H. Du, and H.-L. Liu, J. Phys. Chem. C **125**, 4322 (2021).
[37] See Supplemental Material at http://link.aps.org/supplemental/10.1103/PhysRevB.108.075113 for the detailed structural, *T*-dependent SXRD analysis and Raman shifts of $Ni_2Te_3O_8$ along with the density functional theory calculations.
[38] M. Wang and A. Navrotsky, Solid State Ionics **166**, 167 (2004).
[39] R. Sankar, G. J. Shu, B. Karunakara Moorthy, R. Jayavel, and F. C. Chou, Dalton Trans. **42**, 10439 (2013).
[40] I. Živković, K. Prša, O. Zaharko, and H. Berger, J. Phys.: Condens. Matter **22**, 056002 (2010).
[41] J. Zupan, D. Kolar, and V. Urbanc, Mater. Res. Bull. **6**, 1353 (1971).
[42] H. C. Wu, K. N. Denisova, D. Menzel, D. C. Kakarla, O. V. Maximova, T. W. Kuo, Z. H. Yang, C. H. Lee, W. H. Li, H. Berger, C. W. Wang, C. K. Chang, Y. C. Chuang, J. Y. Lin, M. Gooch, C. W. Chu, A. N. Vasiliev, and H. D. Yang, Phys. Rev. B **100**, 245119 (2019).
[43] A. Pal, T. W. Kuo, C.-H. Hsu, D. C. Kakarla, A. Tiwari, M. C. Chou, A. Patra, P. Yanda, E. Blundo, A. Polimeni, A. Sundaresan, F. C. Chuang, and H. D. Yang, Phys. Rev. B **105**, 024420 (2022).
[44] D. C. Kakarla, H. C. Wu, D. J. Hsieh, P. J. Sun, G. J. Dai, J. Y. Lin, J. L. Her, Y. H. Matsuda, L. Z. Deng, M. Gooch, C. W. Chu, and H. D. Yang, Phys. Rev. B **99**, 195129 (2019).
[45] E. Kroumova, M. I. Aroyo, J. M. Perez-Mato, A. Kirov, C. Capillas, S. Ivantchev, and H. Wondratschek, Phase Transitions **76**, 155 (2003).
[46] F. Kagawa, K. Miyagawa, and K. Kanoda, Nature (London) **436**, 534 (2005).
[47] A. Taroni, S. T. Bramwell, and P. C. W. Holdsworth, J. Phys.: Condens. Matter **20**, 275233 (2008).
[48] R. S. Silva, Jr., J. Gainza, C. dos Santos, J. E. F. S. Rodrigues, C. Dejoie, Y. Huttel, N. Biskup, N. M. Nemes, J. L. Martínez,

N. S. Ferreira, and J. A. Alonso, Chem. Mater. **35**, 2439 (2023).

[49] A. K. Bera, S. M. Yusuf, L. Keller, F. Yokaichiya, and J. R. Stewart, Phys. Rev. B **105**, 014410 (2022).

[50] K. Marty, P. Bordet, V. Simonet, M. Loire, R. Ballou, C. Darie, J. Kljun, P. Bonville, O. Isnard, P. Lejay, B. Zawilski, and C. Simon, Phys. Rev. B **81**, 054416 (2010).

[51] G. Lucazeau, J. Raman Spectrosc. **34**, 478 (2003).

[52] M. Mączka, M. L. Sanjuán, A. F. Fuentes, K. Hermanowicz, and J. Hanuza, Phys. Rev. B **78**, 134420 (2008).

[53] S. Saha, S. Singh, B. Dkhil, S. Dhar, R. Suryanarayanan, G. Dhalenne, A. Revcolevschi, and A. K. Sood, Phys. Rev. B **78**, 214102 (2008).

[54] S. Saha, D. V. S. Muthu, S. Singh, B. Dkhil, R. Suryanarayanan, G. Dhalenne, H. K. Poswal, S. Karmakar, S. M. Sharma, A. Revcolevschi, and A. K. Sood, Phys. Rev. B **79**, 134112 (2009).

[55] B. Poojitha, K. Rubi, S. Sarkar, R. Mahendiran, T. Venkatesan, and S. Saha, Phys. Rev. Mater. **3**, 024412 (2019).

[56] P. G. Klemens, Phys. Rev. **148**, 845 (1966).

[57] M. Balkanski, R. F. Wallis, and E. Haro, Phys. Rev. B **28**, 1928 (1983).

[58] D. J. Lockwood and M. G. Cottam, J. Appl. Phys. **64**, 5876 (1988).

[59] D. J. Lockwood, Low Temp. Phys. **28**, 505 (2002).

[60] A. Nonato, B. S. Araujo, A. P. Ayala, A. P. Maciel, S. Yanez-Vilar, M. Sanchez-Andujar, M. A. Senaris-Rodriguez, and C. W. A. Paschoal, Appl. Phys. Lett. **105**, 222902 (2014).

[61] B. Poojitha, A. Rathore, A. Kumar, and S. Saha, Phys. Rev. B **102**, 134436 (2020).

[62] E. Granado, A. García, J. A. Sanjurjo, C. Rettori, I. Torriani, F. Prado, R. D. Sánchez, A. Caneiro, and S. B. Oseroff, Phys. Rev. B **60**, 11879 (1999).

[63] R. B. Macedo Filho, A. P. Ayala, and C. W. de Araujo Paschoal, Appl. Phys. Lett. **102**, 192902 (2013).

[64] K. D. Truong, M. P. Singh, S. Jandl, and P. Fournier, Phys. Rev. B **80**, 134424 (2009).

[65] P. K. Pandey, R. J. Choudhary, D. K. Mishra, V. G. Sathe, and D. M. Phase, Appl. Phys. Lett. **102**, 142401 (2013).

[66] A. Pal, C. H. Huang, T. W. Yen, P. H. Lee, Y. H. Chang, C. H. Yeh, T. W. Kuo, A. Tiwari, D. C. Kakarla, S. M. Huang, M. C. Chou, H. S. Kunwar, S. Rana, V. G. Sathe, B. H. Chen, Y. C. Chuang, and H. D. Yang, Phys. Rev. B **106**, 094404 (2022).

[67] A. B. Sushkov, O. Tchernyshyov, W. Ratcliff II, S. W. Cheong, and H. D. Drew, Phys. Rev. Lett. **94**, 137202 (2005).

[68] J. S. Lee, T. W. Noh, J. S. Bae, I.-S. Yang, T. Takeda, and R. Kanno, Phys. Rev. B **69**, 214428 (2004).

[69] B. Poojitha, A. Rathore, and S. Saha, J. Magn. Magn. Mater. **483**, 212 (2019).

[70] R. D. Mero, K. Ogawa, S. Yamada, and H.-L. Liu, Sci. Rep. **9**, 18164 (2019).

[71] S. Mukherjee, A. Garg, and R. Gupta, J. Phys.: Condens. Matter **23**, 445403 (2011).

[72] D. Kumar, S. Kumar, and V. G. Sathe, Solid State Commun. **194**, 59 (2014).

[73] C. Meyer, V. Roddatis, P. Ksoll, B. Damaschke, and V. Moshnyaga, Phys. Rev. B **98**, 134433 (2018).

[74] R. Rawat, D. M. Phase, and R. J. Choudhary, J. Magn. Magn. Mater. **441**, 398 (2017).

[75] Y. Tian, M. J. Gray, H. Ji, R. J. Cava, and K. S. Burch, 2D Mater. **3**, 025035 (2016).

[76] C. Xie, L. Shi, J. Zhao, S. Zhou, Y. Li, and X. Yuan, J. Appl. Phys. **120**, 155302 (2016).

[77] E. Aytan, B. Debnath, F. Kargar, Y. Barlas, M. M. Lacerda, J. X. Li, R. K. Lake, J. Shi, and A. A. Balandin, Appl. Phys. Lett. **111**, 252402 (2017).

[78] S. Calder, J. H. Lee, M. B. Stone, M. D. Lumsden, J. C. Lang, M. Feygenson, Z. Zhao, J. Q. Yan, Y. G. Shi, Y. S. Sun, Y. Tsujimoto, K. Yamaura, and A. D. Christianson, Nat. Commun **6**, 8916 (2015).

[79] X. K. Chen, J. C. Irwin, and J. P. Franck, Phys. Rev. B **52**, R13130 (1995).

[80] G. Lawes, A. P. Ramirez, C. M. Varma, and M. A. Subramanian, Phys. Rev. Lett. **91**, 257208 (2003).

[81] M. Hoffmann, K. Dey, J. Werner, R. Bag, J. Kaiser, H. Wadepohl, Y. Skourski, M. Abdel-Hafiez, S. Singh, and R. Klingeler, Phys. Rev. B **104**, 014429 (2021).

[82] K. Dey, S. Sauerland, B. Ouladdiaf, K. Beauvois, H. Wadepohl, and R. Klingeler, Phys. Rev. B **103**, 134438 (2021).

[83] A. Sethi, T. Byrum, R. D. McAuliffe, S. L. Gleason, J. E. Slimak, D. P. Shoemaker, and S. L. Cooper, Phys. Rev. B **95**, 174413 (2017).

[84] T. Katsufuji, S. Mori, M. Masaki, Y. Moritomo, N. Yamamoto, and H. Takagi, Phys. Rev. B **64**, 104419 (2001).

[85] J. W. Kim, S. Artyukhin, E. D. Mun, M. Jaime, N. Harrison, A. Hansen, J. J. Yang, Y. S. Oh, D. Vanderbilt, V. S. Zapf, and S. W. Cheong, Phys. Rev. Lett. **115**, 137201 (2015).